Accepted Manuscript

Low-speed preconditioning for strongly coupled integration of Reynolds-averaged Navier-Stokes equations and two-equation turbulence models

M.S. Campobasso, M. Yan, A. Bonfiglioli, F.A. Gigante, L. Ferrari et al.

PII: S1270-9638(18)30023-3
DOI: https://doi.org/10.1016/j.ast.2018.03.015
Reference: AESCTE 4469

To appear in: *Aerospace Science and Technology*

Received date: 4 January 2018
Revised date: 9 March 2018
Accepted date: 9 March 2018

Low-speed preconditioning for strongly coupled integration of Reynolds-averaged Navier-Stokes equations and two-equation turbulence models

M.S. Campobasso[a,*], M. Yan[a], A. Bonfiglioli[b], F.A. Gigante[c], L. Ferrari[d], F. Balduzzi[e], A. Bianchini[e]

[a] *University of Lancaster, Department of Engineering. Engineering Building, Gillow Avenue, Lancaster LA1 4YW, United Kingdom.*
[b] *University of Basilicata, School of Engineering, Viale dell'Ateneo Lucano 10, 85100 Potenza, Italy*
[c] *University of Glasgow, School of Engineering. James Watt Building South, University Avenue, Glasgow G12 8QQ, United Kingdom.*
[d] *University of Pisa, Department of Energy, Systems, Territory and Construction Engineering, Largo Lucio Lazzarino, 56122 Pisa, Italy*
[e] *University of Florence, Department of Industrial Engineering, Via di Santa Marta 3, 50139 Firenze, Italy*

Abstract

Computational fluid dynamics codes using the density-based compressible flow formulation of the Navier-Stokes equations have proven to be very successful for the analysis of high-speed flows. However, solution accuracy degradation and, for explicit solvers, reduction of the residual convergence rates occur as the local Mach number decreases below the threshold of 0.1. This performance impairment worsens remarkably in the presence of flow reversals at wall boundaries and unbounded high-vorticity flow regions. These issues can be resolved using low-speed preconditioning, but there exists an outstanding problem regarding the use of this technology in the strongly coupled integration of the Reynolds-averaged Navier-Stokes equations and two-equation turbulence models, such as the $k-\omega$ shear stress transport model. It is not possible to precondition only the RANS equations without altering parts of the governing equations, and

*Corresponding author
Email addresses: `m.s.campobasso@lancaster.ac.uk` (M.S. Campobasso), `m.yan@lancaster.ac.uk` (M. Yan), `aldo.bonfiglioli@unibas.it` (A. Bonfiglioli), `mr.fabiogigante@gmail.com` (F.A. Gigante), `lorenzo.ferrari@unipi.it` (L. Ferrari), `balduzzi@vega.de.unifi.it` (F. Balduzzi), `bianchini@vega.de.unifi.it` (A. Bianchini)

there did not exist an approach for preconditioning both the RANS and the SST equations. This study solves this problem by introducing a turbulent low-speed preconditioner of the RANS and SST equations that does not require any alteration of the governing equations. The approach has recently been shown to significantly improve convergence rates in the case of a one-equation turbulence model. The study focuses on the explicit multigrid integration of the governing equations, but most algorithms are applicable also to implicit integration methods. The paper provides all algorithms required for implementing the presented turbulent preconditioner in other computational fluid dynamics codes. The new method is applicable to all low- and mixed-speed aeronautical and propulsion flow problems, and is demonstrated by analyzing the flow field of a Darrieus wind turbine rotor section at two operating conditions, one of which is characterized by significant blade/vortex interaction. Verification and further validation of the new method is also based on the comparison of the results obtained with the developed density-based code and those obtained with a commercial pressure-based code.

Keywords: Reynolds-averaged Navier-Stokes equations, Turbulent low-speed preconditioning, Shear Stress Transport turbulence model, Darrieus wind turbine aerodynamics, Blade/vortex interaction

1. Introduction

Computational fluid dynamics (CFD) codes using the density-based compressible flow formulation of the Euler and Navier-Stokes equations have proven to be very successful for the analysis of high-speed flows. Many flow problems of engineering interest, however, include regions of both high and low fluid speeds. Other than typical aeronautical and turbomachinery examples, such as the flow field past helicopters in slow forward flight, and the transonic flow of high-pressure turbine stages including low-speed labyrinth seal leakage flows, low- and high-speed regions also occur in horizontal axis wind turbine flows, characterized by nearly stagnating flow around the blade root and the turbine nacelle, and speeds close to compressible/incompressible boundary near the rotor tip. In these problem types, the choice of a density-based CFD solver is also very well suited [1]. However, the solution accuracy of these codes decreases in the presence of low-speed flow regions where the local Mach number drops below the threshold of 0.1 [2]. This is due primarily to improper scaling of the numerical dissipation components as the local Mach number tends to zero (incompressible flow limit) [3, 4]. When solving the density-based compressible flow equations using iterative integration methods with a CFL constraint (*e.g.* explicit methods), low flow speeds also result in a significant reduction of the residual convergence rate. In inviscid and, to a significant extent, also in high-Reynolds number flows, this occurs because of the large disparity of acoustic and convective speeds. The CFL constraint imposes maximum time-steps based on the positive acoustic speed, which is the eigenvalue of the convective flux Jacobian with the largest magnitude. As a consequence, numerical errors propagating at the much lower convective speeds are reduced more slowly than numerical errors propagating at acoustic speeds, as the time step imposed by the acoustic eigenvalue is very small with respect to that based on the convective eigenvalue.

Low-speed preconditioning (LSP) [5] can resolve the accuracy issue by restoring the balance of all terms appearing in the matrix-valued numerical dissipation in the incompressible flow limit, and can greatly improve the converge rate by substantially reducing the disparity of acoustic and convective speeds. Indeed, the re-equalization of the characteristic speeds yields convergence rates which, for inviscid and relatively simple viscous flow problems, are independent of the Mach number [6, 7].

Several preconditioning matrices for the Euler and Navier-Stokes equations have been proposed [4, 8, 9]. The main practical difference among most of these preconditioners is their condition number, *i.e.* the ratio between the magnitude of the maximum and minimum eigenvalues of the preconditioned convective flux Jacobian. The condition number of most preconditioners is found to be of order 1 [6], and it is thus likely that these preconditioners may result in comparable residual convergence rates for a given baseline CFD code.

Most LSP strategies were initially developed for the Euler equations; viscous flow effects are usually accounted for by suitable alterations of a preconditioning parameter appearing in the definition of the preconditioning matrix and depending on local flow properties [10, 6, 11]. Some researchers also developed LSP approaches based on preconditioning separately the convective and diffusive flux Jacobians [12]. LSP has been extended to compressible turbulent flow analyses using the Reynolds-averaged Navier-Stokes (RANS) equations and differential turbulent eddy viscosity models. For example, the one-equation Spalart-Allmaras model [13] was used in [14], the $k - \epsilon$ two-equation model [15] was used in [16], the variant of Wilcox's $k - \omega$ two-equation model reported in [17] was used in [18] and [19], and Menter's $k - \omega$ Shear Stress Transport (SST) two-equation model [20] was used in [1].

An important and often overlooked issue arises when using LSP in the framework of the so-called *strongly coupled* integration of the RANS equations and two-equation turbulence model in which the first transport equation expresses the conservation of the turbulent kinetic energy (TKE). With the strongly coupled integration, the RANS and turbulence model equations are solved concurrently at each step of the iterative [21, 22] or direct [23] solution process. Some studies [21] have shown this integration approach to yield higher convergence rates than the *loosely coupled* or *segregated* approach [24], in which the mean flow and turbulence equations are solved in a time-staggered fashion. In the case of low-speed flows, an additional question arises, namely whether LSP may be applied only to the RANS equations or should be applied also to the turbulence model. A recent study addressing this issue for the strongly coupled integration of the RANS equations and the Spalart-Allmaras turbulence model shows that applying LSP also to the turbulent model results in significant improvements of the convergence rate [25]. The present study highlights that in the case of two-equation turbulence models, it is impossible not to precondition the turbulence model without altering parts of the governing equations, and it presents a novel turbulent low-speed preconditioner for the strongly coupled integration approach based on this type of turbulence models. The presented turbulent precondtioner does not require any alteration of the governing equations, was thoroughly validated in [26], and was successfully used for the turbulent low-speed flow analyses of horizontal axis wind turbine blade sections of [1].

The discussion below on the construction of the numerical dissipation for strongly coupled solvers of the RANS and two-equation turbulence model equations is relevant to both explicit and implicit codes. The considered fully coupled integration approach is the explicit multigrid integration of the finite volume structured multi-block COSA code [27, 28, 29], which uses the $k-\omega$ SST model for the turbulence closure. The paper provides all the information required to implement this approach in other CFD codes. The main numerical results reported herein refer to the time-dependent COSA analysis of a Darrieus vertical axis wind turbine (VAWT) rotor at two operating conditions, and these results are also compared to those of a state-of-the-art pressure-based code for further verification and validation of the new turbulent LSP approach. Many more validation analyses of the new LSP approach are available in [26].

The governing equations are provided in Section 2, while the space discretization and the numerical integration of COSA are reported in Section 3, which also reports on the construction of the numerical dissipation in the strongly coupled integration. The LSP method in the strongly coupled integration is presented in Section 4. A validation study based on the analysis of a turbulent flat plate boundary layer is provided in Section 5. The Darrieus rotor section constituting the main test case of this study is defined in Section 6, and the CFD analyses of two operating conditions of this rotor, one of which characterized by a computationally challenging blade/vortex interaction, are presented in Section 7. Summary and conclusions are provided in Section 8.

2. Governing equations

The system of conservation laws considered herein is made up of the compressible RANS equations and the two transport equations of Menter's shear stress transport turbulence model [20]. Given a moving control volume $\mathcal{C}$ with time-dependent boundary $S(t)$, the Arbitrary Lagrangian-Eulerian integral form of the system of the time-dependent RANS and SST equations is:

$$\frac{\partial}{\partial t}\left(\int_{\mathcal{C}(t)} \mathbf{U}\, d\mathcal{C}\right) + \oint_{S(t)} (\underline{\mathbf{\Phi}}_c - \underline{\mathbf{\Phi}}_d) \cdot d\underline{S} - \int_{\mathcal{C}(t)} \mathbf{S}\, d\mathcal{C} = 0 \tag{1}$$

The array $\mathbf{U}$ of conservative flow variables is defined as: $\mathbf{U} = [\rho\ \rho\underline{v}^T\ \rho E\ \rho k\ \rho\omega]^T$ where ρ and $\underline{v}$ are respectively the fluid density and velocity vector, and E, k and ω are respectively the total energy, the turbulent kinetic energy and the specific dissipation rate of turbulent kinetic energy, all per unit mass. The total energy E is given by the sum of the internal energy e, the kinetic energy of the mean flow, and the turbulent kinetic energy k, and its expression is thus:

$$E = e + (\underline{v} \cdot \underline{v})/2 + k \tag{2}$$

For the considered perfect gas case, the static pressure p is given by:

$$p = (\gamma - 1)\rho\,[E - (\underline{v} \cdot \underline{v})/2 - k] \tag{3}$$

The generalized convective flux vector $\underline{\mathbf{\Phi}_c}$ is:

$$\begin{array}{llll} \underline{\mathbf{\Phi}_c} = [& \rho(\underline{v} - \underline{v}_b) & \rho(\underline{v} - \underline{v}_b)\underline{v}^T + pI_{pd} & \rho H(\underline{v} - \underline{v}_b) \\ & & \rho k(\underline{v} - \underline{v}_b) & \rho\omega(\underline{v} - \underline{v}_b)]^T \end{array} \tag{4}$$

where the superscript ^{T} denotes the transpose operator, $\underline{v}_b$ is the velocity of the boundary S, $H = E + p/\rho$ is the total enthalpy per unit mass, and I_{pd} is the identity matrix of dimension pd, the problem dimensionality. The generalized diffusive flux vector $\underline{\mathbf{\Phi}}_d$ depends primarily on the sum of the molecular stress tensor, proportional to the strain rate tensor $\underline{\underline{s}}$, and the turbulent Reynolds stress tensor. Adopting Boussinesq's approximation, the latter tensor is also proportional to $\underline{\underline{s}}$ through an eddy viscosity μ_T. In the SST model, μ_T depends on ρ, k, ω, the vorticity, and the distance from the nearest wall boundary.

The only nonzero entries of the source term $\mathbf{S}$ are those of the k and ω equations, given respectively by:

$$S_k = \mu_T P_d - \frac{2}{3}(\nabla \cdot \underline{v})\rho k - \beta^* \rho k\omega$$

$$S_\omega = \gamma \rho P_d - \frac{2}{3}(\nabla \cdot \underline{v}) \frac{\gamma \rho k}{\nu_T} - \beta \rho \omega^2 + CD_\omega$$

with

$$P_d = 2 \left[\underline{\underline{s}} - \frac{1}{3} \nabla \cdot \underline{v} \right] \nabla \underline{v}$$

$$CD_\omega = 2(1 - F_1) \rho \sigma_{\omega 2} \frac{1}{\omega} \nabla k \cdot \nabla \omega$$

where $\nu_T = \mu_T/\rho$, $\sigma_{\omega 2}$ is a constant, F_1 is a flow state- and wall distance-dependent function, and σ_k, σ_ω, γ, β^* and β are weighted averages of corresponding constants of the standard $k - \omega$ and $k - \epsilon$ models with weights F_1 and $(1 - F_1)$, respectively [20].

Further detail on the formulation of the governing equations can be found in [29] and [30].

3. Numerical method

3.1. Space discretization

COSA solves System (1) with a cell-centered finite volume scheme based on structured multi-block grids. The discretization of the diffusive fluxes and the turbulent source terms is based on second order finite-differencing [29]. The discretization of the convective fluxes of both the RANS and SST partial differential equations (PDEs) uses Van Leer's second order $MUSCL$ extrapolations, Roe's flux-difference splitting, and the Van Albada's flux limiter. Denoting by $\underline{n}$ the outward normal of the face of a grid cell, and dS the area of such a face, the numerical approximation to the continuous convective flux component $\mathbf{\Phi}_{cf} = (\underline{\mathbf{\Phi}_c} \cdot \underline{n})dS$ through the face is:

$$\mathbf{\Phi}^*_{cf} = \frac{1}{2} \left[\mathbf{\Phi}_{cf}(\mathbf{U}_L) + \mathbf{\Phi}_{cf}(\mathbf{U}_R) - \left| \frac{\partial \mathbf{\Phi}_{cf}}{\partial \mathbf{U}} \right| \delta \mathbf{U} \right] \tag{5}$$

The superscript *, the subscript $_f$, and the subscripts $_L$ and $_R$ denote numerical approximation, face value, and value extrapolated from left and the right of the face, respectively. The numerical dissipation depends on the generalized flux Jacobian $\partial \mathbf{\Phi}_{cf}/\partial \mathbf{U}$ and the flow state discontinuity across each cell face, defined by $\delta\mathbf{U} = (\mathbf{U}_R - \mathbf{U}_L)$. Since the RANS and SST equations are solved concurrently, using the strongly coupled approach [21, 22], the Jacobian $\partial\mathbf{\Phi}_{cf}/\partial\mathbf{U}$ has dimension $(pd+4)\times(pd+4)$. When using this approach, the flux differences (*i.e.* the numerical dissipation) of the k and ω equations depend not only on the discontinuities of these two variables at the cell faces, but also on the discontinuities of the RANS variables; less expectedly, the flux difference of the total energy equation depends also on the discontinuities of the turbulent kinetic energy δk. The δk term in the numerical dissipation of the total energy equation is due to the k term in the expression of the total energy given by Eq. (2). The convective flux Jacobian matrix for two-dimensional (2D) problems and the associated expression of the upwind flux differences are provided in Appendix A, and the δk contribution to the numerical dissipation of the total energy equation is the boxed term in Eq. (A6). When using the strongly coupled integration, the coupling of the total energy and the TKE equations makes it impossible to decouple the numerical dissipation of the total energy equation from that of the turbulence model even when no LSP is used. This feature is key to the following discussion on the preconditioned fully coupled integration.

For steady problems the time-derivative appearing in Eq. (1) vanishes; space-discretizing all remaining terms on a given computational grid yields a system of nonlinear algebraic equations of the form:

$$\mathbf{R}_\Phi(\mathbf{Q}) = 0 \tag{6}$$

The entries of the array $\mathbf{Q}$ are the unknown flow variables at the grid cell centers, and the array $\mathbf{R}_\Phi$ stores the cell residuals.

3.2. Integration of steady equations

System (6), representing the discretized RANS and SST equations, is solved with an explicit strongly coupled approach. The RANS and SST equations are time-marched simultaneously until the sought steady state is reached. A fictitious time-derivative $(d\mathbf{Q}/d\tau)$ premultiplied by a diagonal matrix V, the nonzero entries of which are the volumes of the grid cells, is added to System (6), and this derivative is then discretized with a four-stage Runge-Kutta (RK) scheme. The convergence rate is enhanced by means of local time-stepping, variable-coefficient central implicit residual smoothing (IRS) and a full-approximation scheme multigrid (MG) algorithm. To further improve convergence, the negative source terms of the turbulence model $-D_k$, $-D_\omega$ and, when the velocity divergence is positive, $-\nabla \cdot \underline{\mathrm{v}}$ are handled with a point-implicit approach [21, 29]. At the m^{th} stage of each RK cycle, the adopted smoother reads

$$\begin{aligned} (I + \alpha_m \Delta\tau A)\mathbf{Q}^m = \mathbf{Q}^0 + \alpha_m \Delta\tau A \mathbf{Q}^{m-1} - \\ \alpha_m \Delta\tau V^{-1} L_{IRS}[\mathbf{R}_\Phi(\mathbf{Q}^{m-1}) + \mathbf{f}_{MG}] \end{aligned} \tag{7}$$

where m is the stage index, α_m is the m^{th} RK coefficient, $\mathbf{Q}^m$ is the current approximation to the solution $\mathbf{Q}$, $\mathbf{Q}^0$ is the approximation to the solution $\mathbf{Q}$ at the beginning of the RK cycle, V denotes the aforementioned diagonal matrix of the cell volumes, $\Delta\tau$ is the local pseudo-time-step, L_{IRS} denotes the IRS operator, and $\mathbf{f}_{MG}$ is the MG forcing function, which is nonzero when the smoother (7) is used on a coarse level after a restriction step. For each cell, matrix A, of dimension $(pd+4) \times (pd+4)$ has only three nonzero entries in its bottom right (2×2) partition, given by:

$$A(5:6, 5:6) = \begin{bmatrix} (\Delta^+ + \beta^* \omega) & \beta^* k \\ 0 & \gamma\Delta^+ + 2\beta\omega \end{bmatrix} \tag{8}$$

in which $\Delta^+ = \max(0, \frac{2}{3}\nabla \cdot \underline{\mathrm{v}})$, and all variables are evaluated at stage $m-1$. The derivation and discussion of Eq. (8) can be found in [29].

3.3. Integration of time-dependent equations

The time-dependent (TD) equations are solved with a dual-time-stepping approach. The physical time-derivative of System (1) is discretized with a second order backward finite-difference. At physical time-level $n+1$, the sought solution $\mathbf{Q}^{n+1}$ is computed by solving the system:

$$\mathbf{R}_g(\mathbf{Q}^{n+1}) = \frac{3\mathbf{Q}^{n+1} - 4\mathbf{Q}^n + \mathbf{Q}^{n-1}}{2\Delta t} V + \mathbf{R}_\Phi(\mathbf{Q}^{n+1}) = 0 \tag{9}$$

where $\mathbf{R}_g$ denotes the residual vector including the source terms associated with the discretization of the physical time-derivative $\partial\mathbf{U}/\partial t$ of Eq. (1), and Δt is the user-given physical time-step. Also for TD problems with moving bodies, the diagonal matrix V containing the cell volumes is independent of time because, in this study, grids undergo only rigid body motion conforming to the prescribed motion of the body. It is noted that the mass matrix that, in general, would arise from the integration of the time-dependent term in Eq. (1) has been lumped into an identity matrix in System (9). This can be done without sacrificing temporal accuracy, owing to the use of a cell-centred formulation [31].

System (9) is solved with an explicit procedure similar to that used for the steady equations. To further improve numerical stability, however, the $\mathbf{Q}^{n+1}$ term resulting from the dicretization of the physical time-derivative is treated implicitly, as suggested in [32]. Thus, the TD-counterpart of the steady smoother (7) is:

$$\begin{aligned}[I + \alpha_m \Delta\tau (1.5/\Delta t I + A)]\, \mathbf{Q}^m = \mathbf{Q}^0 + \alpha_m \Delta\tau (1.5/\Delta t I + A)\mathbf{Q}^{m-1} - \\ \alpha_m \Delta\tau V^{-1} L_{IRS}[\mathbf{R}_g(\mathbf{Q}^{m-1}) + \mathbf{f}_{MG}]\end{aligned} \tag{10}$$

where $\mathbf{Q}^m$ is shorthand for $\mathbf{Q}^{n+1,m}$. For each cell, the top left $(pd+2)\times(pd+2)$ partition of the matrix premultiplying $\mathbf{Q}^m$ in Algorithm (10) is diagonal, and the bottom right (2×2) partition is upper triangular, due to the matrix pattern highlighted by Eq. (8). Similarly to the case of the integration of the steady equations, this structure enables a decoupled (*i.e.* matrix-free) update of each RANS and SST variable, although ω needs to be updated before k due to the triangular structure of matrix A.

4. Low-speed preconditioning in strongly coupled integration

At low flow speeds, the accuracy loss due to improper scaling of the numerical dissipation and, for the explicit integration, the reduction of the covergence rate due the charasteristic speed disparity can be greatly alleviated by using LSP, the main effects of which are restoring a proper scaling of the numerical dissipation in the incompressible flow limit, and replacing the physical sound speed with a modified or artificial sound speed of magnitude comparable to the convective speeds.

In this study, the strongly coupled turbulent LSP approach for two-equation turbulence models was developed following the steps outlined in [6], but the inviscid/viscous laminar kernel of the new turbulent preconditioner is that proposed by Weiss and Smith [16]. That preconditioner was previously successfully used for solving steady/unsteady inviscid and viscous laminar flows with the COSA code [7, 33, 2], and the turbulent preconditioner presented below was used for the analyses of [1].

4.1. Numerical dissipation

To build the preconditioned algorithm, the fictitious time-derivative $d\mathbf{Q}/d\tau$ used to time-march both the steady and the TD equations is premultiplied by a preconditioning matrix $(\Gamma_c)^{-1}$. By doing so, the system of ordinary differential equations obtained after space-discretizing System (1) takes the form:

$$(\Gamma_c)^{-1}\frac{d\mathbf{Q}}{d\tau} + \mathbf{R}(\mathbf{Q}) = 0 \tag{11}$$

where $\mathbf{R} = \mathbf{R}_\Phi$ for steady problems (see Eq. (6)) and $\mathbf{R} = \mathbf{R}_g$ for TD problems (see Eq. (9)). The introduction of LSP modifies the artificial dissipation appearing in the convective flux defined by Eq. (5) as follows:

$$\mathbf{\Phi}^*_{cf} = \frac{1}{2}\left[\mathbf{\Phi}_{cf}(\mathbf{U}_L) + \mathbf{\Phi}_{cf}(\mathbf{U}_R) - \Gamma_c^{-1}\left|\Gamma_c\frac{\partial \mathbf{\Phi}_{cf}}{\partial \mathbf{U}}\right|\delta\mathbf{U}\right] \tag{12}$$

In the explicit strongly coupled MG solution of the RANS and SST equations, the residual array $\mathbf{R}$ obtained by imposing the flux balance of the modified convective fluxes of Eq. (12), the diffusive fluxes, and the turbulent source terms are premultiplied by the matrix Γ_c before updating the solution on the current grid level to preserve the numerical stability of the scheme [34]. The expression of the preconditioning matrix Γ_c and its inverse $(\Gamma_c)^{-1}$ are reported in Appendix B.

Both matrix Γ_c and its inverse $(\Gamma_c)^{-1}$ depend on the preconditioning parameter M_p. The choice $M_p = 1$ yields no preconditioning, since this choice results in both matrices reducing to the identity matrix. In low-speed flow analyses, instead, COSA uses the baseline definition of the preconditioning parameter proposed in [6], namely:

$$M_p = \min\left(\max\left(M, M_{pg}, M_{vis}, M_{uns}, \epsilon\right), 1\right) \tag{13}$$

where M is the local Mach number, M_{pg} is a cut-off value based on the local pressure gradient [14, 35], M_{vis} is a viscous cut-off value [2], and ϵ is a small cut-off parameter that prevents $(\Gamma_c)^{-1}$ from becoming singular where $M_p = 0$. The parameter M_{uns} is a cut-off value based on the physical time-step Δt and the characteristic lengths of the domain [6]. In the case of TD problems with fixed and moving grids, an effective modification of the LSP approach described above named *mixed preconditioning* was developed and tested in COSA [7, 2] and shown to further improve solution accuracy of low-speed analyses. The design of the preconditiong parameter for low-speed viscous problems has a strong impact on the convergence rate and accuracy of preconditioned solvers, and recent improvements were reported in [11, 25].

When using the strongly coupled integration of the RANS and SST equations, it is mathematically impossible to apply LSP only to the RANS equations because the numerical dissipation of the total energy equation depends on the TKE cell face discontinuities also when no LSP is used, as explained in subsection 3.1 and highlighted by Eq. (A6). Therefore, since the unpreconditioned strongly coupled numerical dissipation is the starting point for constructing the LSP-enhanced strongly coupled approach, preconditioning also the turbulence model is mandatory. This problem was first reported in [6]. These authors attempted to generalize the inviscid preconditioner of [8] to a fully coupled RANS solver using the $k-\epsilon$ model, but reported that this resulted in the eigenvalues of the preconditioned operator $\Gamma_c^{-1}\left|\Gamma_c \partial \mathbf{\Phi}_{cf} \partial \mathbf{U}\right|$ becoming complex. This issue was circumvented by including a mean turbulent pressure depending on TKE in the definition of the sound speed. This results in the removal of the TKE term in the total energy equation, which enables decoupling the numerical dissipation of the total energy and TKE equations, and thus use the fully coupled integration removing the need for preconditioning the turbulence model. This approach, however, raises concerns about the solution uncertainty due to the alteration of parts of the governing equations. Equally importantly, preconditioning the turbulence model has recently been shown to significantly improve the convergence rate of the strongly coupled integration using one-equation models [8]. For these reasons, it becomes important to develop a preconditioned fully-coupled approach for two-equation turbulence models.

The contruction of the preconditioner of [8] starts by formulating the Euler equations in non-conservative form with respect to the set of primitive variables $\mathbf{V}_p^i = [p \quad \underline{\mathrm{v}}^T \quad T]^T$ [6], with T denoting the fluid static temperature. One then constructs the Jacobian matrix $\overline{\Gamma}_p^{-1} = \partial \mathbf{U}^i / \partial \mathbf{V}_p^i$, with $\mathbf{U}^i = [\rho \quad \rho\underline{\mathrm{v}}^T \quad \rho E]^T$. Choi and Merkle obtained the preconditioner $(\Gamma_p^{-1})_{CM}$ [8] referred to the non-conservative form of the Euler equations written in terms of the $\mathbf{V}_p^i$ variables by suitably modifying the derivative $\partial\rho/\partial p$ and setting to zero the derivative $\partial\rho/\partial T$ [6]. Weiss and Smith obtained the preconditioner $(\Gamma_p^{-1})_{WS}$ [16] by modifying the derivative $\partial\rho/\partial p$ in $\overline{\Gamma}_p^{-1}$ as done in [8] but retained the derivative $\partial\rho/\partial T$ [6]. The authors of the present study found that turbulent LSP for the strongly coupled integration can be obtained by generalizing the preconditioning approach of [16]. To obtain real eigenvalues of the preconditioned convective flux Jacobian, preserving the hyperbolic character of the convective part of the governing equations, it is necessary to retain all occurrences of $\partial\rho/\partial T$ in the preconditioner. The sought turbulent preconditioner Γ_p^{-1} referred to the non-conservative form of the RANS and SST equations written with respect to the primitive variables $\mathbf{V}_p = [p \quad \underline{\mathrm{v}}^T \quad T \quad k \quad \omega]^T$ is:

$$
{\Gamma_p}^{-1} = \begin{bmatrix}
\frac{1+\gamma_1 M_p^2}{a^2\gamma M_p^2} & 0 & 0 & -\frac{\rho}{a^2} & 0 & 0 \\
\frac{(1+\gamma_1 M_p^2)u}{a^2\gamma M_p^2} & \rho & 0 & -\frac{\rho u}{a^2} & 0 & 0 \\
\frac{(1+\gamma_1 M_p^2)v}{a^2\gamma M_p^2} & 0 & \rho & -\frac{\rho v}{a^2} & 0 & 0 \\
\frac{2a^2+\zeta(1+\gamma_1 M_p^2)}{2a^2\gamma\gamma_1 M_p^2} & \rho u & \rho v & -\frac{\rho\zeta}{2\gamma_1 a^2} & \rho & 0 \\
\frac{(1+\gamma_1 M_p^2)k}{a^2\gamma M_p^2} & 0 & 0 & -\frac{\rho k}{a^2} & \rho & 0 \\
\frac{(1+\gamma_1 M_p^2)\omega}{a^2\gamma M_p^2} & 0 & 0 & -\frac{\rho\omega}{a^2} & 0 & \rho
\end{bmatrix} \tag{14}
$$

where, $\gamma_1 = \gamma - 1$, $\delta_2 = 1 - M_p^2$, $q^2 = u^2 + v^2$, $\zeta = \gamma_1(q^2 + 2k)$ and $a^2 = \gamma_1(H - q^2/2 - k)$ is the sound speed squared.

It is noted that no coupling of the RANS and turbulence model, in addition to that due to the eddy viscosity linking the turbulence model to the mean flow equations via the Reynolds stress tensor in the momentum and total energy equations, occurs when using one-equation turbulence models [25]. In this circumstance, one may choose whether to precondition or not the turbulence model when using a strongly coupled integration.

The expression of the preconditioned eigenvalues and flux differences are reported in Appendix B. An interesting feature emerging from comparing the expressions of the unpreconditioned flux difference of the total energy equation provided by Eq. (A6) and its preconditioned counterpart provided by Eq. (B6) is that the expression of the δk term is independent of whether LSP is used or not. However, the residual preconditioning before the solution update, required for numerical stability [4] results in the precondtioned numerical dissipation of the total energy equation containing contribution of all flux differences.

It is also noted that with LSP all characteristic-based boundary conditions undergo alterations because two characteristics are altered by the introduction of LSP [36], as highlighted by Equations (B11) and (B12) of Appendix B.

4.2. Integration of time-dependent equations

The point-implicit MG iteration to solve turbulent low-speed TD problems is obtained following the derivation for the viscous laminar case reported in [2], and reads:

$$\begin{aligned}\left[I + \alpha_m \Delta\tau \Gamma_c (1.5/\Delta t I + A)\right] \mathbf{Q}^m = \quad & \mathbf{Q}^0 + \alpha_m \Delta\tau \Gamma_c (1.5/\Delta t I + A) \mathbf{Q}^{m-1} - \\ & \alpha_m \Delta\tau V^{-1} \Gamma_c L_{IRS} [\mathbf{R}_g(\mathbf{Q}^{m-1}) + \mathbf{f}_{MG}]\end{aligned} \tag{15}$$

For each cell, the matrix premultiplying $\mathbf{Q}^m$ is dense due to the structure of the preconditioner Γ_c highlighted by Eq. (B1). Therefore the update process requires the inversion of a $(pd+4) \times (pd+4)$-matrix for each grid cell. The steady

MG solver is retrieved by setting to zero the terms proportional to $1.5/\Delta t$ and replacing $\mathbf{R}_g$ with $\mathbf{R}_\phi$ in Algorithm (15).

As customary with explicit CFD schemes with LSP, calculating the local time-step using the maximum preconditioned acoustic speed (value obtained with the + sign in Eq. (B16)) rather than the corresponding unpreconditioned speed (value obtained with the + sign in Eq. (A17)) yields significant convergence acceleration at low flow speeds, and, for relatively simple problems, independence of the convergence rate on the Mach number [2].

5. Verification and validation

Demonstration of the second order spatial and temporal accuracy of COSA and validation of its predicting capabilities were reported in [37, 2, 33, 29, 30]; the code was recently validated for 3D steady and TD horizontal axis wind turbine flows [38], and used also for 3D hydrodynamic analyses of oscillating wings for tidal energy applications [28]. A comprehensive validation of the presented turbulent preconditioner, including low-speed COSA analyses of a backward facing step, a wall-mounted hump, a curved wall boundary layer interacting with a cross-flow jet and two airfoils, is available in [26].

Here, the turbulent LSP-enhanced code is verified and validated by considering the turbulent boundary layer over a flat plate for several values of M_∞. The analyses below are carried out with COSA and are an improved and extended version of those first reported in [1].

5.1. turbulent flat plate

A flat plate turbulent boundary layer at a Reynolds number Re of 6×10^6 based on a unitary plate length and the freestream velocity is considered herein. The computational domain is rectangular and the plate lies on the lower horizontal boundary. The plate leading edge (LE) is at the origin of the Cartesian system, and the trailing edge (TE) is at $x = 1$, where the (vertical) outlet boundary is positioned. The inlet boundary is at $x = -1/3$, and the upper horizontal side is a far field boundary at $y = 1$. The Cartesian grid used for the analyses below has 384 cells along y, whose height increases from the lower to the upper boundary starting from a minimum value of $2.5 \cdot 10^{-7}$. The grid has 256 equal intervals along x; 192 are on the flat plate and 64 between the LE and the inlet boundary. A mesh refinement analysis showed that the solution computed with the grid defined above is mesh-independent. All simulations discussed below have been performed using the so-called *improved auxiliary state* far field BCs for internal flows [37] on the left and right boundaries of the domain, and a standard external-flow characteristic-based far field condition on the top boundary. Symmetry conditions are imposed on the portion of the lower boundary between the inlet boundary and the plate LE, and a no-slip condition is applied on the flat plate.

To assess the effectiveness of the developed turbulent LSP technique, this test case has been solved for three values of M_∞, namely 0.1, 0.01 and 0.001, and for each value a simulation with LSP and one without have been performed. In all cases, the freestream turbulence intensity has been set to 0.1 percent, and the freestream value of the ratio of turbulent and laminar viscoisty has been set to 0.11. From a physical standpoint, the effects of compressibility are expected to be negligible for M_∞ of order 0.1 or less, and therefore CFD analyses using $M_\infty \leq 0.1$ should yield the same solution, represented in suitable nondimensional form.

The three profiles of the nondimensionalized velocity component parallel to the flat plate on a line orthogonal to the flat plate itself at $x = 0.5$, computed with and without LSP are reported in the left and right subplot of Fig. 1 respectively (the label 'NP' in the top left corner of the right subplot denotes simulations performed without LSP). The variable on the x-axis is the logarithm in base 10 of y^+, the nondimensionalized wall distance, defined as $y^+ = (u_\tau y)/\nu_w$, where u_τ and ν_w are the friction velocity and the wall kinematic viscosity respectively. The variable on the y-axis is u^+, the nondimensionalized velocity component $u_\parallel$ parallel to the wall, which, in this case, is the x-component of the velocity vector. Its expression is $u^+ = u_\parallel/u_\tau$. Both subplots also report

Spalding's profile, which is a power-series interpolation of experimental data joining the linear sublayer to the logarithmic region of the turbulent boundary layer occurring on a flat plate in the absence of a streamwise pressure gradient. The left plot of Fig. 1 shows that the three LSP-based solutions for the three values of M_∞ are superimposed, as expected, and in very good agreement with Spalding's profile. The right plot of Fig. 1 shows that the CFD solutions without LSP are not independent of the Mach number, as the solution associated with $M_\infty = 0.001$ differs both from the other two CFD results and Spalding's estimate.

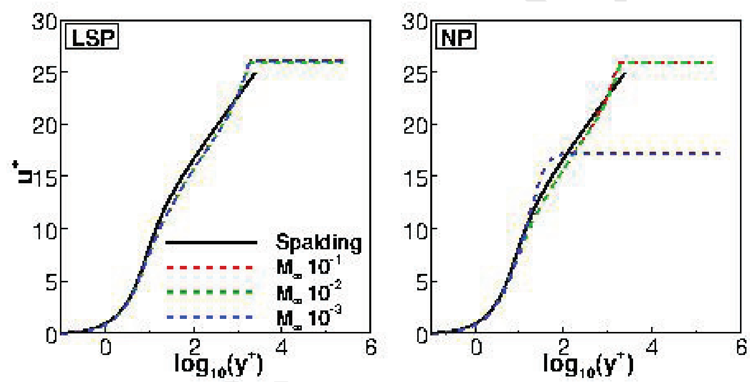

Figure 1: Turbulent flat plate boundary layer: comparison of Spalding's velocity profile and velocity profiles of CFD simulations with $M_\infty = 0.1$, $M_\infty = 0.01$ and $M_\infty = 0.001$. Left: COSA solutions with LSP; right: COSA solutions without LSP.

The values of the drag coefficient C_d obtained with the three LSP simulations and the three simulations not using LSP are reported in the second and third columns of Table 1, respectively. These data emphasize that the C_d predicted by the LSP analysis tends to a constant value of 3.12×10^{-3} as M_∞ decreases. Conversely, the drag coefficient estimate of the analysis without LSP does not converge to a constant value as M_∞ is reduced, due to the numerical errors associated with the numerical dissipation imbalance at low Mach number. A theoretical C_d value of 3.20×10^{-3} for the considered configuration is obtained

Table 1: Turbulent flat plate boundary layer: comparison of drag coefficient extracted from COSA simulations with $M_\infty = 0.1$, $M_\infty = 0.01$ and $M_\infty = 0.001$ with and without LSP.

M_∞	LSP	NP
$1 \cdot 10^{-1}$	3.11×10^{-3}	3.20×10^{-3}
$1 \cdot 10^{-2}$	3.12×10^{-3}	6.99×10^{-3}
$1 \cdot 10^{-3}$	3.12×10^{-3}	34.0×10^{-3}

using the semi-empirical relation

$$C_d = \frac{0.523}{log^2(0.06Re)}$$

reported in [39]. The difference of about 2.5 % between the theoretical estimate and LSP-enabled CFD result is deemed quite good, because within the uncertainty margin affecting the semi-empirical model.

The contours of the static pressure coefficient C_p around the flat plate LE obtained for the three values of M_∞ are depicted in the six plots of Fig. 2. The definition of the plotted coefficient is:

$$C_p = \frac{p' - p'_\infty}{0.5M_\infty^2}$$

where p' is the static pressure nondimensionalized by the product of the freestram density and sound speed squared. The top plots of Fig, 2 provide the C_p contours of the three LSP-based solutions, and the bottom ones those without LSP. The top plots highlight that the use of LSP yields solutions independent of M_∞, as expected on the basis of physical evidence, whereas the bottom plots underline that the resolution of the pressure field past the LE, the region where the strongest gradient of this variable occurs, becomes increasingly poor as M_∞ decreases.

The comparative solution analyses just discussed provide one more example of the necessity of using LSP to preserve the accuracy of the solution when solving low-speed flows with the compressible density-based CFD codes. They also provide a first verification and validation step of the new turbulent LSP

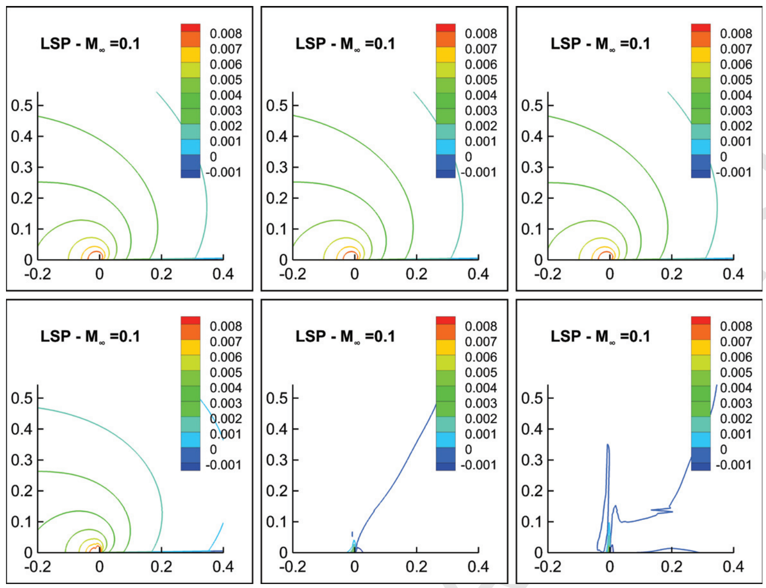

Figure 2: Turbulent flat plate boundary layer: comparison of contours of pressure coefficient C_p computed by COSA with and without LSP. Left: solutions for $M_\infty = 0.1$; middle: solutions for $M_\infty = 0.01$; right: solutions for $M_\infty = 0.001$.

method presented in the paper, confirming the correctness and robustness of its implementation.

All simulations have been run for $4,000$ MG cycles with three grid levels and $CFL = 3$. The COSA residual convergence histories with and without LSP for the three considered values of M_∞ are reported in the six plots of Fig. 3, which provides the convergence histories of the continuity equation (plot labeled ρ), the $x-$component of the momentum equation (plot labeled ρu), the $y-$component of the momentum equation (plot labeled ρv), the energy equation (plot labeled ρE), the turbulent kinetic energy equation (plot labeled ρk), and the specific dissipation rate equation (plot labeled $\rho\omega$). In all plots, the variable on the x-axis is the number of multigrid iterations, and the variable Δl_r on the y-axis is the logarithm in base 10 of the RMS of the cell residuals of the considered PDE normalized by the value of such RMS after the first MG cycle. Inspection of the residual histories of the RANS and the ω equations highlights that both the convergence rate and the overall residual drop of all three LSP simulations is independent of M_∞, as expected on the basis of theoretical analyses. The general pattern of the convergence history of the k equation of the three LSP simulations is also independent of M_∞, but the overall drop of the residuals of this equations decreases as M_∞ decreases. This possibly occurs because of finite (double) precision of the simulations, and the growing level of cancellation errors affecting the convective flux balances as M_∞ decreases. This is because the magnitude of convective fluxes of k depends on M_∞^3, due to the dependence of the background level of k on the square of the mean freestream velocity. Fig. 3 also shows that both the convergence rate and the overall drop of all residual of the simulations without LSP worsens as M_∞ decreases, due to the increasing disparity between acoustic and convective speeds.

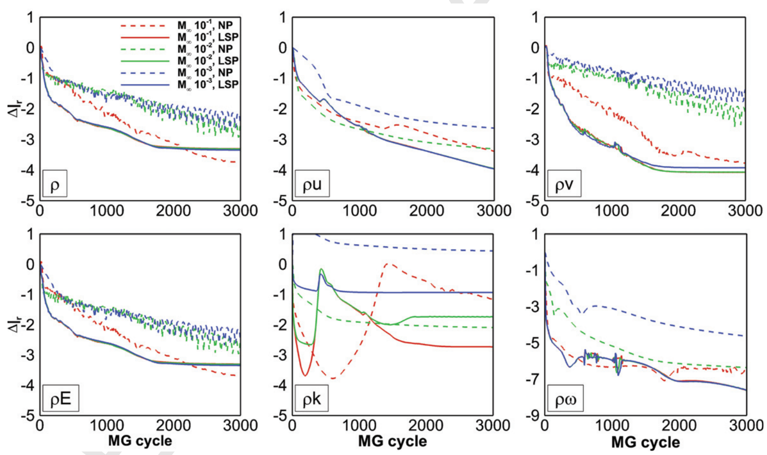

Figure 3: Turbulent flat plate boundary layer: comparison of COSA residual convergence histories with and without LSP for $M_\infty = 0.1$, $M_\infty = 0.01$ and $M_\infty = 0.001$.

6. H-Darrieus rotor section

The main test case used herein to assess the effectiveness of the turbulent LSP algorithm presented above is the periodic flow of a H-Darrieus wind turbine rotor section. The blade airfoils of this turbine type are stacked along straight lines parallel to the turbine rotational axis. Away from the blade tips, the flow can be considered two-dimensional. The considered 3-blade rotor section has radius R_D of 515 mm, and the blades use the NACA0021 airfoil with a chord c of 85.8 mm. The blade/spoke attachment is at 25 % chord from the airfoil leading edge. Two operating conditions are analyzed in Section 7, and they differ only because of the value of the so-called tip-speed ratio (TSR). Denoting by Ω_D the rotor angular speed, the TSR definition is:

$$\lambda_D = \frac{\Omega_D R_D}{W_\infty}$$

Both operating conditions are characterized by a freestream velocity W_∞ of 9 m/s, and they differ only for the rotor speed, which is 480 RPM ($\lambda_D = 2.88$) in one case, and 440 RPM ($\lambda_D = 2.64$) in the other. Using a reference density of 1.21 Kg/m^3, a reference temperature of 288 K, the rotor circumferential speed as reference velocity and the airfoil chord as reference length, the Reynolds number at $\lambda_D = 2.88$ is 1.52×10^5, and that at $\lambda_D = 2.64$ is 1.39×10^5. The flow field of this rotor section at $\lambda_D = 3.3$ was analyzed in [40] and [27], where the COSA code was used without LSP. The schematic of the considered rotor section (not in scale) is depicted in Fig. 4.

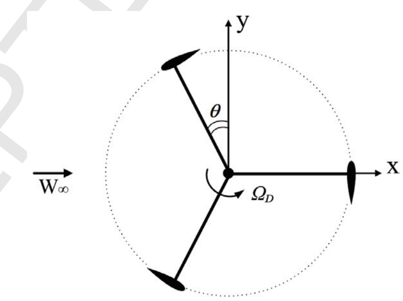

Figure 4: Schematic of three-blade Darrieus rotor section.

VAWT rotor flows are inherently unsteady because the freestream conditions perceived by each blade vary periodically, with frequency determined by the rotor angular speed. Starting by temporarily neglecting the fact that the absolute velocity decreases across the rotor due to the energy transferred from the fluid to the turbine, the modulus of the relative wind velocity $\underline{W}^r_\infty$ at the rotor radius R_D, and the angle ϕ^r_∞ between W^r_∞ and the time-dependent position of the airfoil chord are respectively:

$$W^r_\infty = W_\infty \sqrt{1 + 2\lambda_D \cos\theta + \lambda_D^2} \tag{16}$$

$$\phi^r_\infty = \arctan\left(\frac{\sin\theta}{\lambda_D + \cos\theta}\right) \tag{17}$$

Here the angle θ defines the azimuthal position of the reference blade. The reference blade has $\theta = 0$ when the directions of the absolute velocity W_∞ and the entrainment velocity $\Omega_D R_D$ are equal and opposite. The periodic profiles of M^r_∞, the Mach number associated with W^r_∞, and ϕ^r_∞ for the two aforementioned TSR values are reported in the left and right plots of Fig. 5, respectively. Both curve sets are plotted with a solid line for $0 < \theta < 180^o$, the interval corresponding to the reference blade traveling upwind, and with a dashed line for $180^o < \theta < 360^o$, the interval corresponding to the reference blade traveling downwind. This distinction is highlighted because Equations. (16) and (17) assume that the absolute velocity W_∞ is constant throughout the rotor. This is an acceptable approximation in the upwind region but is unacceptable in the downwind region. This is because the energy transfer occurring in the upwind region results in a reduction of the absolute velocity, yielding in turn a significant reduction of both W^r_∞ and ϕ^r_∞ in the downwind region.

The left plot of Fig. 5 reports the curves of the relative freestream Mach number M^r_∞ for the considered TSR values. This variable is obtained by dividing Eq. (16) by the sound speed. The plot shows that the minimum values of M^r_∞, achieved at $\theta \approx 180^o$, are below 0.05. In this position, the Reynolds number based on the relative flow velocity also achieves its minimum, resulting in thicker boundary layer increasing the effective airfoil thickness and chordwise pressure gradients and causing a larger extent of flow separation. The minimum relative Mach number decreases as TSR decreases. The curves of the right plot of Fig. 5 show that the peak values of the relative angle of attack (AoA) ϕ^r_∞ increase with TSR, a circumstance that results in progressively higher levels of dynamic stall as TSR decreases. The observations above highlight that the flow complexity increases as TSR is reduced.

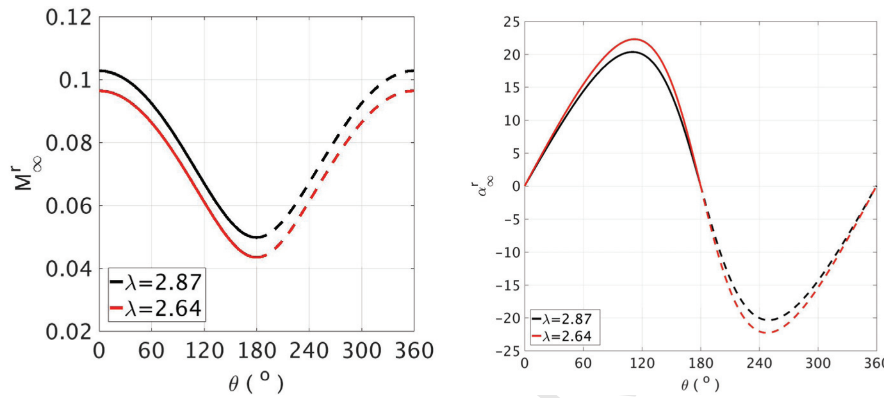

Figure 5: Left: variation of relative freestream Mach number during one rotor revolution. Right: variation of AoA during one rotor revolution.

7. Results

Here the flow field past the Darrieus rotor section defined above at $\lambda_D = 2.88$ and $\lambda_D = 2.64$ is analyzed with both the density-based COSA code, and the pressure-based ANSYS® FLUENT® code, denoted FLUENT below for brevity. The COSA simulations use the multigrid integration approach discussed above, and are carried out both with and without LSP to highlight the solution accuracy improvements achievable by using LSP, and all density-based solutions are compared to the FLUENT pressure-based solutions for further cross-validation. The pressure-based solutions have been performed using the FLUENT *coupled* integration approach, whereby the momentum and the pressure-based continuity equations are solved in a fully-coupled fashion. The SST transport equations are instead integrated in a segregated or loosely coupled fashion.

The same computational grid, already shown to deliver grid-independent solutions with both codes [40], is used for all analyses discussed below.

7.1. physical and numerical set-up

The physical domain containing the rotor section and its surroundings is delimited by a far field boundary centered at the rotor axis, and is discretized by a structured multi-block grid. The grid is highly clustered in the region around and between the blades, has 729,600 quadrilateral cells and is made up of two subdomains: the circular region of radius $7R_D$ containing the three blades and consisting of 522,240 cells, and the annular region with inner radius of $7R_D$ and outer radius of $240R_D$ consisting of 207,360 cells. The grid features 448 cells around each airfoil, and a distance of the first grid line off the airfoil surface from the airfoil itself of $10^{-5}c$. Enlarged views of the grid around the rotor and the airfoil are reported respectively in the left and right images of Fig. 6.

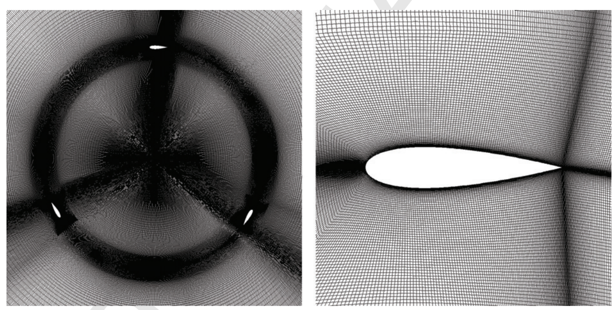

Figure 6: Darrieus rotor section. Left: grid in rotor region; right: grid in airfoil region.

The identification of two distinct subdomains is irrelevant for the COSA analyses since the entire grid moves with the rotor. The circular interface between the two subdomains was introduced to also enable the simulation of this rotor flow with FLUENT using the same grid of COSA. FLUENT uses a rotating and a stationary domain and requires a circular sliding interface, which was set to be the circle at distance $7R_D$ from the rotor center. The FLUENT results presented below are obtained with the coupled pressure-based solver [41]. All COSA and FLUENT simulations do not use transition modeling and are fully turbulent. In all cases, the far field values of k and ω are determined by considering a turbulence intensity of 5 percent and a characteristic turbulence length of 70 mm.

All COSA simulations discussed below have been performed using the MG solver with 3 grid levels. No CFL ramping has been used, and the CFL number has been set to 4.

7.2. density-based and pressure-based CFD analysis

In order to assess the impact of using LSP on the solution quality of the density-based code, the flow fields and the predicted performance associated with $\lambda_D = 2.64$ and $\lambda_D = 2.88$ are considered. Both regimes are analyzed with COSA and FLUENT. The simulations of the TSR 2.88 regime used 360 time-intervals per period (TD 360), and those of the TSR 2.64 regime used 720 time-intervals per period, since these choices were found to yield time-step-independent solutions.

The periodic profiles of the overall torque coefficient computed by COSA with and without LSP, and FLUENT at $\lambda_D = 2.88$ are reported in Fig. 7. The variable θ on the x-axis is the circumferential position of the reference blade, whereas the definition of the torque coefficient on the y-axis is:

$$C_t = \frac{T(\theta)}{0.5 \rho_\infty W_\infty^2 A R_D}$$

in which T is the rotor torque on the reference blade due to both pressure and viscous forces, and A is the frontal area of the rotor. In the 2D simulations analyzed below, T is torque per unit blade length and $A = 2R_D$. Fairly small differences exist between the density-based solutions obtained with and without LSP, the most noticeable ones occurring around $\theta = 150^o$. The overall small differences between these two results indicate that at this relatively high TSR the use of LSP may not be essential for accurately predicting blade forces and rotor torque. One also notes that the pressure-based solution predicts higher torques between the peak value at $\theta \approx 90^o$ and the lowest value at $\theta \approx 180^o$. This points to a faster stall recovery of the pressure-based solution after the occurrence of stall towards the peak value of the torque. As shown below, this discrepancy increases as λ_D decreases. The origin of these differences is still uncertain, and possible causes include slight differences in the implementation of the turbulence model in the two codes. As an example, COSA determines the value of the specific dissipation rate at wall boundaries ω_w using the following expression proposed in [20]:

$$\omega_w = \frac{60\nu_w}{\beta\Delta_w^2} \tag{18}$$

where Δ_w is the distance to the next grid point away from the wall. The expression of ω_w reported in the FLUENT theory manual is structurally different from that of Eq. (18). Performing some transformations (not reported herein for brevity) aiming to obtain comparable expressions of ω_w in the two codes, it has been found that the value of ω_w used by FLUENT is about one order of magnitude smaller than that used by COSA, a difference which may contribute to the differences between the two simulation sets. In fact, the COSA analyses of an attached flat plate turbulent boundary layer reported in [29] show that ω_w variations of this order alter the value of the wall viscous stress, giving a difference of about 4 % in the predicted viscous drag. In the same report, it is also shown that, in the case of a stalled flow regime of the NACA4412 airfoil, the aforementioned variation level of ω_w results in a variation of the total drag of about 12 %. Verification of the impact of the ω_w boundary condition discrepancy on the differences between the COSA and FLUENT VAWT solutions reported herein will be further investigated in follow-on studies. It is noted, however, that it may not be possible to achieve conclusive answers due to the source code of FLUENT not being publically available.

The vorticity contours of the density-based solution without and with LSP, and those of the pressure-based solution past the rotor at $\theta = 140^o$ for $\lambda_D = 2.88$ are reported respectively in Figures 8-(a), 8-(b) and 8-(c). It is noticed that the LSP-enhanced solution has smoother contours than that of the density-based code without LSP, and the former solution appears to have less diffusion of the wakes. The LSP solution is also significantly closer to the pressure-based solution. This provides a first indication of the improvements of the solution

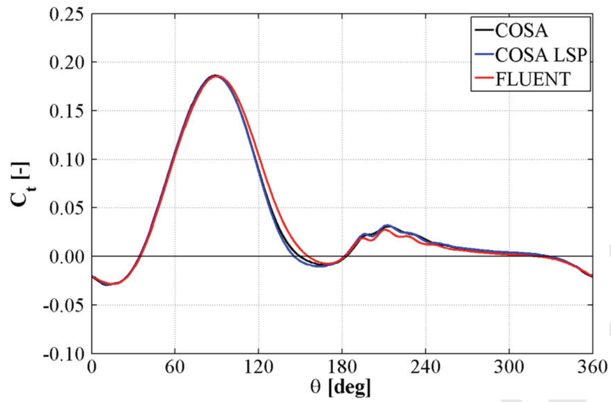

Figure 7: Overall torque coefficient predicted by COSA without and with LSP and FLUENT at $\lambda_D = 2.88$.

quality of the density-based code achievable by using the presented LSP method.

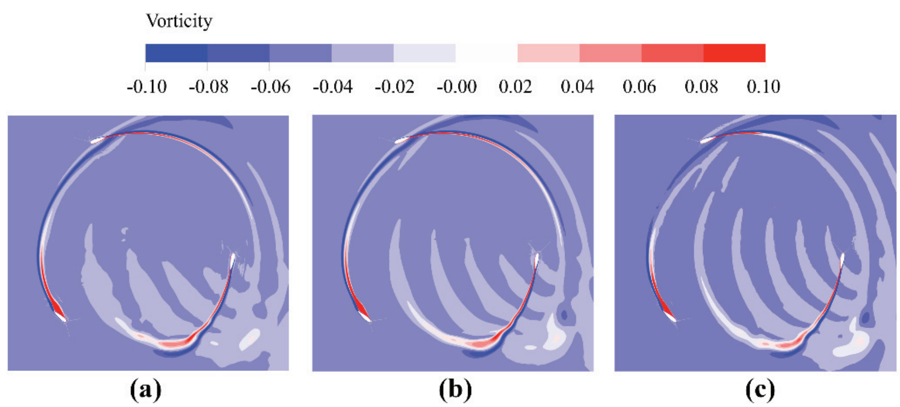

Figure 8: Vorticity contours at $\theta = 140^o$ for $\lambda_D = 2.88$: (a) COSA without LSP, (b) COSA with LSP, and (c) FLUENT.

595 The periodic C_t profiles computed by COSA with and without LSP, and FLUENT at $\lambda_D = 2.64$ are reported in Fig. 9. Unlike the higher TSR case, significant differences exist between the density-based solutions obtained with

and without LSP. Such differences are particularly large in the interval $130^o < \theta < 240^o$, the range of azimuthal positions characterized by the lowest flow speeds of the revolution, as shown in the left plot of Fig. 5, and where the use of LSP in the density code is thus expected to yield more accurate estimates than the unpreconditioned solver. It is noted, however, that the flow velocity level in this interval is not significantly different from that in the same range of angular positions at $\lambda_D = 2.88$, indicating additional flow complexity at $\lambda_D = 2.88$. This aspect will be further investigated below. It is also noted that the LSP-enhanced density-based solution is extremely close to the pressure-based solution in the interval $140^o < \theta < 240^o$, which provides further evidence of the predictive capabilities of the density-based code enhanced by the proposed LSP method. Both density-based solutions agree fairly well with the pressure-based prediction until the end of the period for $240^o < \theta < 360^o$. Also in the present 2.64 TSR case, the lower torque coefficient of both COSA predictions with respect to the FLUENT prediction in the interval $90^o < \theta < 130^o$ indicate a delay of stall recovery of the density-based code with respect to the pressure-based code, confirming that this phenomenon is unaffected by LSP. As previously mentioned, this discrepancy may be due to small variations in the implementation of the turbulence model in the two codes.

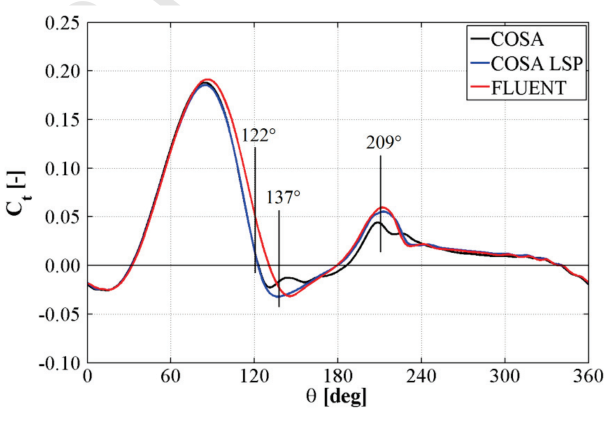

Figure 9: Overall torque coefficient predicted by COSA without and with LSP and by FLUENT at $\lambda_D = 2.64$.

The torque coefficient profiles of Fig. 9 highlight that for $\lambda_D = 2.64$ the agreement among the three simulations varies significantly with the angular position of the rotor. To investigate in greater depth these variations, a more detailed comparison of the three predictions is carried out for the three angular positions highlighted in Fig. 9, namely for values of θ of 122^o, 137^o and 209^o. The relative Mach number contours of the density-based solution without and with LSP, and those of the pressure-based solution past the reference blade at $\theta = 122^o$ are depicted respectively in the left, middle and right images of Fig. 10. Fairly small differences are observed between the density-based solution without and with LSP, whereas both solutions differ significantly from the pressure-based prediction. The density-based solutions predict a larger recirculation zone due to stall on the blade suction side (SS). As highlighted by the pressure torque profiles of Fig. 9, this is due to the density-based code predicting a delayed stall recovery following the stall onset at the peak torque achieved at $\theta \approx 90^o$.

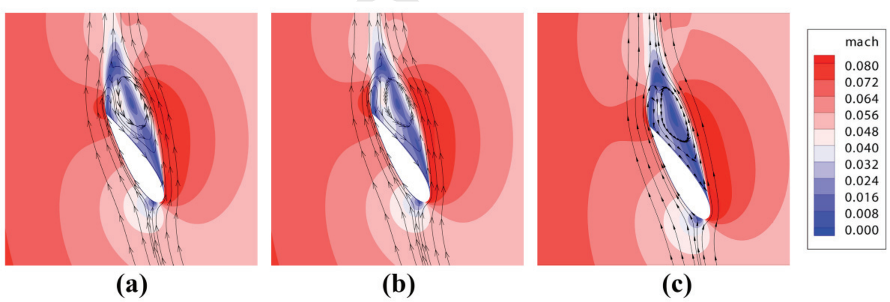

Figure 10: Relative Mach number contours at $\theta = 122^o$ for $\lambda_D = 2.64$: (a) COSA without LSP, (b) COSA with LSP and (c) FLUENT.

The blade pressure coefficient C_p and skin friction coefficient C_f predicted by the three analyses at $\theta = 122^o$ are compared in Fig. 11-(a) and 11-(b) respectively. The definitions of these two parameters are:

$$C_p = \frac{p_w - p_\infty}{0.5\rho_\infty (W_\infty^r)^2}$$

$$C_f = \frac{|\tau_w|}{0.5\rho_\infty (W_\infty^r)^2}$$

where p_w and τ_w denote respectively static pressure and viscous stress at the airfoil surface, and the relative freestream velocity W_∞^r is defined by Eq. (16). The C_p profiles of Fig. 11-(a) highlight negligible differences of blade loading between the two density-based simulations, as expected on the basis of the torque coefficient equality at this circumferential position highlighted in Fig. 9. More noticeable differences between the loading of the density-based and the pressure-based solutions are instead observed. The higher pressure on the SS in the first 20 percent of the blade predicted by the density-based code indicates a stronger leading-edge separation in this region. The lower pressure between 60 percent chord and the trailing edge is due to the higher speed associated with the stronger stall-induced recirculation predicted by the density-based code. As highlighted in Fig. 11-(b), the position of the suction side separation predicted by the two codes is the same and is defined by the SS C_f cusp at about 4 % of the chord. These profiles also reveal that the position of the reattachment point on the SS shortly before the trailing edge is the same for all simulations. The main difference between the density- and pressure-based simulations is the strength of the separation, due to different stall recovery rates.

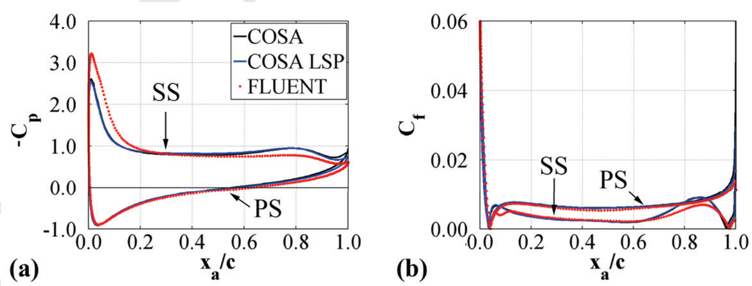

Figure 11: Predictions of (a) blade pressure coefficient and (b) skin friction coefficient of COSA without and with LSP and FLUENT at $\theta = 122^o$ for $\lambda_D = 2.64$.

The vorticity contours of the density-based solution without and with LSP, and those of the pressure-based solution past the reference blade at $\theta = 137^o$

for $\lambda = 2.64$ are depicted respectively in the left, middle and right images of Fig. 12. The region with red contours corresponds to a large counterclockwise vortex above the SS induced by stall, whereas the smaller region with blue contours corresponds to an induced clockwise vortex. Large differences are observed between the density-based solutions without LSP (Fig. 12-(a)) and that with LSP (Fig. 12-(b)), particularly in the resolution of the main counterrotating vortex. Conversely, the latter solution is significantly closer to the pressure-based prediction (Fig. 12-(c)). This is a remarkable result since the comparison of the overall torque profiles of Fig. 9 shows that at $\theta = 137^o$ the torque coefficients of the density-based code without LSP and the pressure-based code are nearly the same, whereas those of the LSP-enhanced density-based code and the pressure-based code differ significantly. This occurrence underlines the importance of considering both integral output functions and local flow variables when carrying out comparative assessments of VAWT analyses based on different numerical and even experimental approaches, since a seemingly good agreement of integral values may be fortuitous.

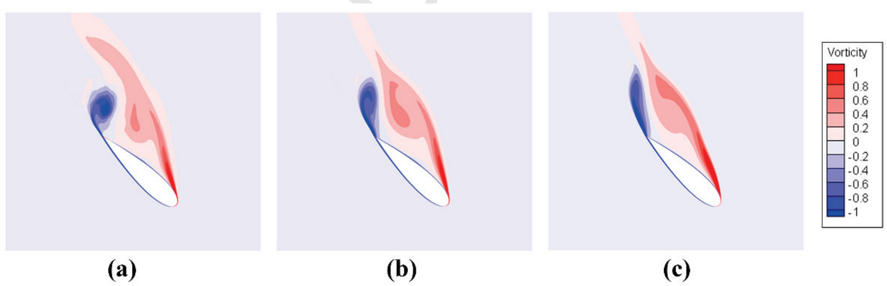

Figure 12: Vorticity contours at $\theta = 137^o$ for $\lambda_D = 2.64$: (a) COSA without LSP, (b) COSA with LSP and (c) FLUENT.

The left, middle and right images of Fig. 13 respectively provide the vorticity contours of the density-based solution without and with LSP, and those of the pressure-based solution past the rotor at $\theta = 209^o$ for $\lambda = 2.64$. An excellent agreement between the LSP-enhanced density-based solution and the pressure-based solution is observed. Both predictions highlight that in this rotor position the reference blade travels through and past strong vortices shed by the blade itself in the upwind and leeward region of its trajectory. The density-based prediction without LSP, conversely, fails to properly resolve the vortex system and the blade/vortex interactions at this angular position. A proper resolution of the shed vortex system and its interactions with the blades is key to the reliable estimation of the blade forces and rotor torque. These results stress the importance of using LSP when analyzing Darrieus wind turbine performance and aerodynamics at low TSR with a density-code, provide further evidence of the effectiveness of the developed LSP method, and also explain the reasons for the excellent agreement of the torque predictions of the LSP-enhanced density-based code and the pressure-based code for $140^o < \theta < 240^o$ observed in Fig. 9.

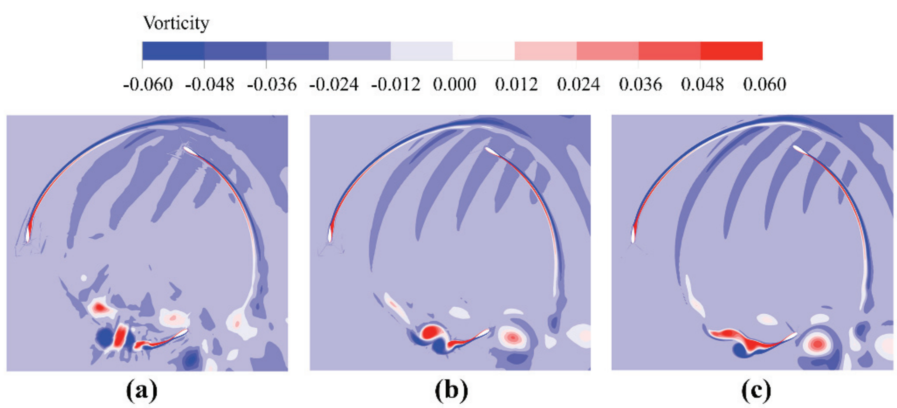

Figure 13: Vorticity contours at $\theta = 209^o$ for $\lambda_D = 2.64$: (a) COSA without LSP, (b) COSA with LSP and (c) FLUENT.

The three predictions of the blade pressure coefficient C_p and skin friction coefficient C_f at $\theta = 209^o$ for $\lambda_D = 2.64$ are compared in Fig. 14-(a) and 14-(b) respectively. One sees that at this angular position of the rotor, the LSP-enhanced density-based and the pressure-based solutions are in excellent agreement and both predict substantially higher loading than the density-based solution without LSP. These observations are fully consistent with the overall torque profiles of Fig. 9, and also the comparative analysis of the vorticity contours of Fig. 13. The static pressure over the first half of the airfoil SS predicted by the density-based solver without LSP is significantly higher than that of the other two analyses. This is because the former simulation fails to adequately resolve the low-pressure region associated with the conterclockwise vortex shed by the airfoil itself, which at this angular position and for this TSR is ahead of the airfoil leading edge on the airfoil outer side (*i.e.* SS). This blade/vortex interaction yielding higher blade load is instead adequately resolved by the other two simulations. It is also observed that this blade/vortex interaction effect has a beneficial effect on the rotor torque. This is highlighted by the fact that the secondary peak of the rotor torque at $\theta \approx 210^o$ for $\lambda_D = 2.88$ (Fig. 7) is lower than that at $\theta = 209^o$ for $\lambda_D = 2.64$ (Fig. 9). The lower pressure on the front portion of the reference blade predicted by COSA with LSP and FLUENT results in higher flow velocity in this region, which yields thinner boundary layers with higher wall viscous stress. This explains why the C_f profiles over the first blade half predicted by these two simulations is higher than that of the COSA analysis without LSP.

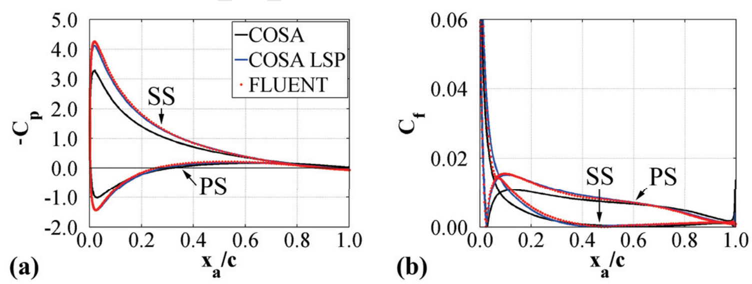

Figure 14: Predictions of (a) blade pressure coefficient and (b) skin friction coefficient of COSA without and with LSP and FLUENT at $\theta = 209^o$ for $\lambda_D = 2.64$.

8. Conclusions

When applying LSP to the strongly coupled integration of the density-based RANS equations and the SST turbulence model equations, it is unavoidable to precondition both the RANS and the turbulence model equations, unless parts of the governing equations are altered, and a case-dependent solution uncertainty is accepted. This contraint stems from the TKE term appearing in the definition of the total energy. The paper has presented and discussed a novel and rigorous turbulent low-speed preconditioner for the considered integration strategy. Applying LSP to the strongly coupled integration of the RANS equations and the one-equation Spalart-Allmaras has recently been shown to significantly improve convergence rates [25], and this improvement is expected to hold also in the SST model case. Unfortunately, however, this improvement cannot be quantified with numerical experiments due to impossibility of implementing the strongly coupled integration by preconditioning only the RANS equations and leaving unaltered all parts of the governing equations.

The turbulent preconditioner has been developed and discussed in the context of the fully coupled explicit integration of the RANS and SST equations of the COSA code, but the presented methodology is applicable to all two-equation turbulence models featuring a transport equation for the turbulent kinetic energy, and also to implicit fully coupled integration methods.

The presented turbulent LSP formulation has been demonstrated by analyzing two flow regimes of a three-blade Darrieus wind turbine rotor section, one at lower loading regime (TSR $\lambda = 2.88$) and the other at higher loading regime (TSR $\lambda = 2.64$), characterized by significant blade/vortex interaction. Both regimes have been analyzed with the baseline density-based code, the turbulent LSP-enhanced code, and the FLUENT pressure-based solver for verification and validation purposes. It was found that the LSP-based solution, unlike that of the baseline density-based solver, provides a very good resolution of the blade/vortex interaction phenomena at $\lambda = 2.64$, due to the high-resolution of low-speed vortical flow regions achievable by using LSP. At $\lambda = 2.88$, a regime characterized by simpler aerodynamics, the beneficial effect of LSP is lower, and the density-based solutions with and without LSP are in better agreement. All LSP-based and pressure-based solutions are in good agreement, and this provides strong evidence of the correctness of the novel turbulent LSP technology and of the solution accuracy enhancement of density-based codes for realistic low-speed problems of engineering interest.

Acknowledgements

The density-based simulations were performed on two clusters. One is the POLARIS cluster, part of the N8 HPC facilities provided and funded by the N8 consortium and EPSRC (Grant No.EP/K000225/1). The other resource is the HEC cluster of Lancaster University, which is also kindly acknowledged. Prof. Ennio Antonio Carnevale and Prof. Giovanni Ferrara of the Universita' degli Studi di Firenze are kindly acknowledged for supporting this project.

Appendix A. Unpreconditioned flux Jacobian and flux differences

For 2D flow problems, the Jacobian of the fluxes normal to a cell face is:

$$\frac{\partial \mathbf{\Phi}_{cf}}{\partial \mathbf{U}} = \begin{bmatrix} 0 & n_x & n_y & 0 & 0 & 0 \\ \frac{\gamma_1}{2} q^2 n_x - uU_n & U_n - n_x\gamma_2 u & n_y u - n_x \gamma_1 v & n_x\gamma_1 & -n_x\gamma_1 & 0 \\ \frac{\gamma_1}{2} q^2 n_y - vU_n & n_x v - n_y\gamma_1 u & U_n - n_y\gamma_2 v & n_y\gamma_1 & -n_y\gamma_1 & 0 \\ \frac{\gamma_1}{2} q^2 U_n - U_n H & n_x H - \gamma_1 u U_n & n_y H - \gamma_1 v U_n & \gamma U_n & -\gamma_1 U_n & 0 \\ -U_n k & n_x k & n_y k & 0 & U_n & 0 \\ -U_n\omega & n_x\omega & n_y\omega & 0 & 0 & U_n \end{bmatrix} \tag{A1}$$

where $q^2 = u^2 + v^2$, $\gamma_2 = \gamma - 2$ and U_n denotes the component of the flow velocity along the outward (with reference to any given grid cell) face normal $\underline{n}$, defined by:

$$U_n = un_x + vn_y \tag{A2}$$

The unpreconditioned flux differences are:

$$\delta f_1 = \alpha_1|\lambda_1| + \alpha_3|\lambda_3| + \alpha_4|\lambda_4| \tag{A3}$$

$$\delta f_2 = \alpha_1 u|\lambda_1| + \alpha_2|\lambda_2|n_y + \alpha_3|\lambda_3|(u + an_x) + \alpha_4|\lambda_4|(u - an_x) \tag{A4}$$

$$\delta f_3 = \alpha_1 v|\lambda_1| - \alpha_2|\lambda_2|n_x + \alpha_3|\lambda_3|(v + an_y) + \alpha_4|\lambda_4|(v - an_y) \tag{A5}$$

$$
\begin{aligned}
\delta f_4 &= (q^2/2 + k)\alpha_1|\lambda_1| + \alpha_2|\lambda_2|U_t \\
&\quad + (H + aU_n)\alpha_3|\lambda_3| + (H - aU_n)\alpha_4|\lambda_4| + \boxed{\alpha_5|\lambda_5|} \qquad \text{(A6)} \\
\delta f_5 &= \alpha_1|\lambda_1|k + \alpha_3|\lambda_3|k + \alpha_4|\lambda_4|k + \alpha_5|\lambda_5| \qquad \text{(A7)} \\
\delta f_6 &= \alpha_1|\lambda_1|\omega + \alpha_3|\lambda_3|\omega + \alpha_4|\lambda_4|\omega + \alpha_6|\lambda_6| \qquad \text{(A8)}
\end{aligned}
$$

where the tangential velocity component U_t is given by:

$$U_t = un_y - vn_x \qquad \text{(A9)}$$

The unpreconditioned characteristic variables α_i are:

$$
\begin{aligned}
\alpha_1 &= \left(\delta\rho - \frac{\delta p}{c^2}\right) && \text{(A10)} \\
\alpha_2 &= \rho\delta U_t && \text{(A11)} \\
\alpha_3 &= \left(\frac{\delta p}{c^2} + \frac{\rho\delta U_n}{c}\right)/2 && \text{(A12)} \\
\alpha_4 &= \left(\frac{\delta p}{c^2} - \frac{\rho\delta U_n}{c}\right)/2 && \text{(A13)} \\
\alpha_5 &= \rho\delta k && \text{(A14)} \\
\alpha_6 &= \rho\delta\omega && \text{(A15)}
\end{aligned}
$$

and the eigenvalues of the Jacobian $\left|\frac{\partial \mathbf{\Phi}_{cf}}{\partial \mathbf{U}}\right|$ are:

$$
\begin{aligned}
|\lambda_{1/2/5/6}| &= |U_n| && \text{(A16)} \\
|\lambda_{3/4}| &= |U_n \pm c| && \text{(A17)}
\end{aligned}
$$

The boxed term in Eq. (A6) is the contribution of the TKE gradient to the numerical dissipation of the total energy equation, due to the TKE term in the definition of the total energy provided by Eq. (2).

Appendix B. Preconditioners and preconditioned flux differences

The expression of the preconditioning matrices Γ_c and its inverse $(\Gamma_c)^{-1}$ are respectively:

$$\Gamma_c = \begin{bmatrix} 1+\frac{\gamma_1\delta_2 q^2}{2a^2} & -\frac{\gamma_1\delta_2 u}{a^2} & -\frac{\gamma_1\delta_2 v}{a^2} & \frac{\gamma_1\delta_2}{a^2} & -\frac{\gamma_1\delta_2}{a^2} & 0 \\ \frac{\gamma_1\delta_2 q^2 u}{2a^2} & 1-\frac{\gamma_1\delta_2 u^2}{a^2} & -\frac{\gamma_1\delta_2 uv}{a^2} & \frac{\gamma_1\delta_2 u}{a^2} & -\frac{\gamma_1\delta_2 u}{a^2} & 0 \\ \frac{\gamma_1\delta_2 q^2 v}{2a^2} & -\frac{\gamma_1\delta_2 uv}{a^2} & 1-\frac{\gamma_1\delta_2 v^2}{a^2} & \frac{\gamma_1\delta_2 v}{a^2} & -\frac{\gamma_1\delta_2 v}{a^2} & 0 \\ \frac{\delta_2 q^2(2a^2+\zeta)}{4a^2} & -\frac{\delta_2 u(2a^2+\zeta)}{2a^2} & -\frac{\delta_2 v(2a^2+\zeta)}{2a^2} & \frac{2a^2M_p^2+\delta_2\zeta}{2a^2} & \delta_2-\frac{\delta_2\zeta}{2a^2} & 0 \\ \frac{\gamma_1\delta_2 q^2 k}{2a^2} & -\frac{\gamma_1\delta_2 uk}{a^2} & -\frac{\gamma_1\delta_2 vk}{a^2} & \frac{\gamma_1\delta_2 k}{a^2} & 1-\frac{\gamma_1\delta_2 k}{a^2} & 0 \\ \frac{\gamma_1\delta_2 q^2\omega}{2a^2} & -\frac{\gamma_1\delta_2 u\omega}{a^2} & -\frac{\gamma_1\delta_2 v\omega}{a^2} & \frac{\gamma_1\delta_2\omega}{a^2} & -\frac{\gamma_1\delta_2\omega}{a^2} & 1 \end{bmatrix} \tag{B1}$$

and

$$(\Gamma_c)^{-1} = \begin{bmatrix} 1-\frac{\gamma_1\delta_2 q^2}{2a^2M_p^2} & \frac{\gamma_1\delta_2 u}{a^2M_p^2} & \frac{\gamma_1\delta_2 v}{a^2M_p^2} & -\frac{\gamma_1\delta_2}{a^2M_p^2} & \frac{\gamma_1\delta_2}{a^2M_p^2} & 0 \\ -\frac{\gamma_1\delta_2 q^2 u}{2a^2M_p^2} & 1+\frac{\gamma_1\delta_2 u^2}{a^2M_p^2} & \frac{\gamma_1\delta_2 uv}{a^2M_p^2} & -\frac{\gamma_1\delta_2 u}{a^2M_p^2} & \frac{\gamma_1\delta_2 u}{a^2M_p^2} & 0 \\ -\frac{\gamma_1\delta_2 q^2 v}{2a^2M_p^2} & \frac{\gamma_1\delta_2 uv}{a^2M_p^2} & 1+\frac{\gamma_1\delta_2 v^2}{a^2M_p^2} & -\frac{\gamma_1\delta_2 v}{a^2M_p^2} & \frac{\gamma_1\delta_2 v}{a^2M_p^2} & 0 \\ -\frac{\delta_2 q^2(2a^2+\zeta)}{4a^2M_p^2} & \frac{\delta_2 u(2a^2+\zeta)}{2a^2M_p^2} & \frac{\delta_2 v(2a^2+\zeta)}{2a^2M_p^2} & \frac{2a^2-\delta_2\zeta}{2a^2M_p^2} & \frac{\delta_2}{M_p^2}+\frac{\delta_2\zeta}{2a^2M_p^2} & 0 \\ -\frac{\gamma_1\delta_2 q^2 k}{2a^2M_p^2} & \frac{\gamma_1\delta_2 uk}{a^2M_p^2} & \frac{\gamma_1\delta_2 vk}{a^2M_p^2} & -\frac{\gamma_1\delta_2 k}{a^2M_p^2} & 1+\frac{\gamma_1\delta_2 k}{a^2M_p^2} & 0 \\ -\frac{\gamma_1\delta_2 q^2\omega}{2a^2M_p^2} & \frac{\gamma_1\delta_2 u\omega}{a^2M_p^2} & \frac{\gamma_1\delta_2 v\omega}{a^2M_p^2} & -\frac{\gamma_1\delta_2\omega}{a^2M_p^2} & \frac{\gamma_1\delta_2\omega}{a^2M_p^2} & 1 \end{bmatrix} \tag{B2}$$

where, $\gamma_1 = \gamma - 1$, $\delta_2 = 1 - M_p^2$, $\zeta = \gamma_1(q^2 + 2k)$ and $a^2 = \gamma_1(H - q^2/2 - k)$ is the sound speed squared.

The six components $\delta f_{i,p}$ of the preconditioned numerical dissipation $\Gamma_c^{-1}\left|\Gamma_c \frac{\partial \mathbf{\Phi}_{cf}}{\partial \mathbf{U}}\right|\delta\mathbf{U}$ are:

$$\delta f_{1,p} = \alpha_1|\lambda_1| + \frac{\alpha_3|\lambda_3|(\lambda_3 - U_n) - \alpha_4|\lambda_4|(\lambda_4 - U_n)}{aM_p^2} \tag{B3}$$

$$\begin{aligned} \delta f_{2,p} &= \alpha_1 u|\lambda_1| + \alpha_2|\lambda_2|n_y + an_x(\alpha_3|\lambda_3| - \alpha_4|\lambda_4|) \\ &\quad + \frac{u\left[\alpha_3|\lambda_3|(\lambda_3 - U_n) - \alpha_4|\lambda_4|(\lambda_4 - U_n)\right]}{aM_p^2} \end{aligned} \tag{B4}$$

$$\begin{aligned} \delta f_{3,p} &= \alpha_1 v|\lambda_1| - \alpha_2|\lambda_2|n_x + an_y(\alpha_3|\lambda_3| - \alpha_4|\lambda_4|) \\ &\quad + \frac{v\left[\alpha_3|\lambda_3|(\lambda_3 - U_n) - \alpha_4|\lambda_4|(\lambda_4 - U_n)\right]}{aM_2^2} \end{aligned} \tag{B5}$$

$$\begin{aligned} \delta f_{4,p} &= (q^2/2 + k)\alpha_1|\lambda_1| + \alpha_2|\lambda_2|U_t \\ &\quad + \left(\frac{\lambda_3 - U_n}{aM_p^2}H + aU_n\right)\alpha_3|\lambda_3| - \left(\frac{\lambda_4 - U_n}{aM_p^2}H + aU_n\right)\alpha_4|\lambda_4| + \boxed{\alpha_5|\lambda_5|} \end{aligned} \tag{B6}$$

$$\delta f_{5,p} = \alpha_1|\lambda_1|k + \frac{\alpha_3|\lambda_3|(\lambda_3 - U_n) - \alpha_4|\lambda_4|(\lambda_4 - U_n)}{aM_p^2}k + \alpha_5|\lambda_5| \tag{B7}$$

$$\delta f_{6,p} = \alpha_1|\lambda_1|\omega + \frac{\alpha_3|\lambda_3|(\lambda_3 - U_n) - \alpha_4|\lambda_4|(\lambda_4 - U_n)}{aM_p^2}\omega + \alpha_6|\lambda_6| \tag{B8}$$

The characteristic variables α_i associated with the preconditioned problem are:

$$\alpha_1 = \delta\rho - \frac{\delta p}{a^2} \tag{B9}$$

$$\alpha_2 = \rho\delta U_t \tag{B10}$$

$$\alpha_3 = \frac{\delta p - \rho\delta U_n(\lambda_4 - U_n)}{a(\lambda_3 - \lambda_4)} \tag{B11}$$

$$\alpha_4 = \frac{\delta p - \rho\delta U_n(\lambda_3 - U_n)}{a(\lambda_3 - \lambda_4)} \tag{B12}$$

$$\alpha_5 = \rho\delta k \tag{B13}$$

$$\alpha_6 = \rho\delta\omega \tag{B14}$$

The eigenvalues of the preconditioned Jacobian $\Gamma_c^{-1}\left|\Gamma_c\frac{\partial\mathbf{\Phi}_{cf}}{\partial\mathbf{U}}\right|$ are:

$$|\lambda_{1/2/5/6}| = |U_n| \tag{B15}$$

$$|\lambda_{3/4}| = \frac{1}{2}\left|U_n(1 + M_p^2) \pm \sqrt{4a^2M_p^2 + (M_p^2 - 1)^2U_n^2}\right| \tag{B16}$$

The boxed term in Eq. (B6) is the contribution of the TKE gradient to the numerical dissipation of the total energy equation, due to the TKE term in the definition of the total energy provided by Eq. (2). This term equals that of the case without preconditioning. It is also noted that a) LSP modifies only the characteristic variables α_3 and α_4, as concluded by comparing Equations (A10)-(A15) and Equations (B9)-(B14), and b) the preconditioned flux differences equal their unpreconditioned counterparts if $M_p = 1$, as expected.

The interested reader is referred to [26] for the the derivation of all expressions presented in this Appendix.

References

[1] M. Campobasso, M. Yan, J. Drofelnik, A. Piskopakis, M. Caboni, Compressible Reynolds-Avergaed Navier-Stokes Analysis of wind Turbine Tur-

bulent Flows Using a Fully Coupled Low-Speed Preconditioned Multigrid Solver, ASME paper GT2014-25562 (June 2014).

[2] M. Campobasso, J. Drofelnik, Compressible Navier-Stokes analysis of an oscillating wing in a power-extraction regime using efficient low-speed preconditioning, Computers and Fluids 67 (2012) 26–40.

[3] E. Turkel, A. Fiterman, B. Van Leer, Preconditioning and the Limit to the Incompressible Flow Equations, in: D. Caughey, M. Hafez (Eds.), Computing the Future: Frontiers of Computational Fluid Dynamics 1994, Wiley Publishing, 1994, pp. 215–234.

[4] E. Turkel, Preconditioning techniques in computational fluid dynamics, Annual Review of Fluid Mechanics 31 (1999) 385–416.

[5] E. Turkel, Preconditioned methods for solving the incompressible and low speed compressible equations, Journal of Computational Physics 72 (1987) 277–298.

[6] S. Venkateswaran, C. Merkle, Analysis of Preconditioning Methods for the Euler and Navier-Stokes Equations, 30th VKI Lecure Series on Computational Fluid Dynamics (May 1999).

[7] M. Campobasso, A. Bonfiglioli, M. Baba-Ahmadi, Development of Efficient and Accurate CFD Technologies for Wind Turbine Unsteady Aerodynamics, in: J. Vad (Ed.), Proceedings of the Conference on Modeling Fluid Flow, Vol. 2 of 14th Event of International Conference Series on Fluid Flow Technologies held in Budapest, Department of Fluid Mechanics, Budapest University of Technology and Economics, 2009, pp. 879–886.

[8] Y. Choi, C. Merkle, The application of preconditioning to viscous flows, Journal of Computational Physics 105 (1993) 207–223.

[9] B. Koren, B. van Leer, Analysis of preconditioning and multigrid for Euler flows with low-subsonic regions, Advances in computational mathematics 4 (1995) 127–144.

[10] P. Buelow, Convergence Enhancement of Euler and Navier-Stokes Algorithms, Ph.D. thesis, Pennsylvania State University, Pennsylvania, USA (December 1995).

[11] Y. Colin, H. Deniau, j.-F. Boussage, A robust low speed preconditioning formulation for viscous flow computations, Computers and Fluids 47 (2011) 1–15.

[12] C. Depcik, B. van Leer., In Search of an Optimal Local Navier-Stokes preconditioner, AIAA paper 2003-3703, 16th AIAA Computational Fluid Dynamics Conference, Orlando, Florida (June 2003).

[13] P. Spalart, S. Allmaras, A one-equation turbulence model for aerodynamic flows, La Recherche Aerospatiale 1 (1994) 5–21.

[14] J. Weiss, J. Maruszewski, W. Smith, Implicit Solution of Preconditioned Navier-Stokes Equations Using Algebraic Multigrid, AIAA Journal 37 (1) (1999) 29–36.

[15] B. Launder, D. Spalding, The Numerical Computation of Turbulent Flow, Computer Methods in Applied Mechanics and Engineering 3 (1974) 269–289.

[16] J. Weiss, W. Smith, Preconditioning applied to variable and constant density flows, AIAA Journal 33 (11) (1995) 2050–2057.

[17] D. Wilcox, Simulation of Transition with a Two-Equation Turbulence Model, AIAA Journal 32 (2) (2004) 247–255.

[18] V. Gleize, A. . Le Pape, Low Mach Number Preconditioning for Unsteady Flow in General ALE Formulation., AIAA paper 2006-687, 44th AIAA Aerospace Sciences Meeting and Exhibit, Reno, Nevada (January 2006).

[19] A. Le Pape, V. Gleize, Improved Navier-Stokes Computations of a Stall-regulated Wind Turbine Using Low Mach Number Preconditioning, AIAA

paper 2006-1502, 44th AIAA Aerospace Sciences Meeting and Exhibit, Reno, Nevada (January 2006).

[20] F. Menter, Two-equation Turbulence-models for Engineering Applications, AIAA Journal 32 (8) (1994) 1598–1605.

[21] F. Liu, X. Zheng, A Strongly Coupled Time-Marching Method for Solving the Navier-Stokes and $K-\omega$ Turbulence Model Equations with Multigrid, Journal of Computational Physics 128 (2) (1996) 289–300.

[22] F. Lin, F. Sotiropoulos, Strongly-Coupled Multigrid Method for 3-D Incompressible Flows Using Near-Wall Turbulence Closures, Journal of Fluids Engineering 119 (1997) 314–324.

[23] A. Bonfiglioli, M. Campobasso, Computing Three-Dimensional Turbomachinery Flows with an Implicit Fluctuation Splitting Scheme, in: T. Lajos, J. Vad (Eds.), Proceedings of the Conference on Modeling Fluid Flow, Vol. 2 of 13th Event of International Conference Series on Fluid Flow Technologies held in Budapest, Department of Fluid Mechanics, Budapest University of Technology and Economics, 2006, pp. 996–1003.

[24] F. Liu, X. Zheng, Staggered Finite Volume Scheme for Solving Cascade Flows with a $K-\omega$ Turbulence Model, AIAA Journal 32 (8) (1994) 1589–1597.

[25] R. Djeddi, J. Howison, K. Ekici, A fully-coupled turbulent low-speed preconditioner for harmonic balance applications, Aerospace Science and Technology 53 (2016) 22–37.

[26] M. Yan, Time-domain and Harmonic Balance Turbulent Navier-Stokes Analysis of Wind Turbine Aerodynamics using a Fully Coupled Low-Speed Preconditioned Multigrid Solver, Ph.D. thesis, Lancaster University, United Kingdom (2015).

[27] M. Campobasso, J. Drofelnik, F. Gigante, Comparative Assessment of the Harmonic Balance Navier-Stokes Technology for Horizontal and Vertical

Axis Wind Turbine Aerodynamics, Computers and Fluids 136 (2016) 345–370.

[28] J. Drofelnik, M. Campobasso, Comparative Turbulent Three-Dimensional Navier-Stokes Hydrodynamic Analysis and Performance Assessment of Oscillating Wings for Renewable Energy A pplications, International Journal of Marine Energy 16 (2016) 100–115.

[29] M. Campobasso, A. Piskopakis, J. Drofelnik, A. Jackson, Turbulent Navier-Stokes Analysis of an Oscillating Wing in a Power-Extraction Regime Using the Shear Stress Transport Turbulence Model, Computers and Fluids 88 (2013) 136–155.

[30] M. Campobasso, F. Gigante, J. Drofelnik, Turbulent Unsteady Flow Analysis of Horizontal Axis Wind Turbine Airfoil Aerodynamics Based on the Harmonic Balance Reynolds-Averaged Navier-Stokes Equations, ASME paper GT2014-25559 (June 2014).

[31] V. Venkatakrishnan, D. Mavriplis, Implicit Method for the Computation of Unsteady Flows on Unstructured Grids, Journal of Computational Physics 127 (2) (1996) 380–397.

[32] N. Melson, D. Sanetrik, H. Atkins, Time-accurate Navier-Stokes Calculations with Multigrid Acceleration, Proc. 6^{th} Copper Mountain Conference on Multigrid Methods (1993) II423–II437.

[33] M. Campobasso, M. Baba-Ahmadi, Analysis of Unsteady Flows Past Horizontal Axis Wind Turbine Airfoils Based on Harmonic Balance Compressible Navier-Stokes Equations with Low-Speed Preconditioning, Journal of Turbomachinery 134 (6).

[34] E. Turkel, R. Radespiel, N. Kroll, Assessment of Preconditioning Methods for Multidimensional Aerodynamics, Computers and Fluids 26 (6) (1997) 613–634.

[35] D. Darmofal, K. Siu, A Robust Multigrid Algorithm for the Euler Equations with Local Preconditioning and Semi-coarsening, Journal of Computational Physics 151 (1999) 728–756.

[36] K. Hejranfar, R. Kamali-Moghadam, Preconditioned characteristic boundary conditions for solution of preconditioned Euler equations at low Mach number flows, Journal of Computational Physics 231 (12) (2012) 4384–4402.

[37] M. Campobasso, M. Baba-Ahmadi, Ad-hoc Boundary Conditions for CFD Analyses of Turbomachinery Problems with Strong Flow Gradients at Farfield Boundaries, Journal of Turbomachinery 133 (4).

[38] J. Drofelnik, Massively Parallel Time- and Frequency-Domain Navier-Stokes Computational Fluid Dynamics Analysis of Wind Turbines and Oscillating Wing Unsteady Flows, Ph.D. thesis, Glasgow University, United Kingdom (2017).

[39] F. White, Viscous Fluid Flow, Third edition, McGraw-Hill, New York, USA, 2006.

[40] F. Balduzzi, A. Bianchini, F. Gigante, G. Ferrara, M. Campobasso, l. Ferrari, Parametric and Comparative Assessment of Navier-Stokes CFD Technologies for Darrieus Wind Turbines Performance Analysis, GT2015-42663 (June 2015).

[41] Ansys-Inc, Fluent theory guide, Tech. Rep. release 14.5 (2013).
URL `https://www.ansys.com/Products/Fluids/ANSYS-Fluent`